Research paper

Multi-layer monoclinic $BiVO_4$ with oxygen vacancies and V^{4+} species for highly efficient visible-light photoelectrochemical applications

Jin-Meng Wu[a,b], Ying Chen[a,b], Lun Pan[a,b,*], Peihong Wang[c], Ya Cui[a,b], DeChao Kong[a], Li Wang[a,b], Xiangwen Zhang[a,b], Ji-Jun Zou[a,b]

[a] Key Laboratory for Green Chemical Technology of the Ministry of Education, School of Chemical Engineering and Technology, Tianjin University, Tianjin 300072, China
[b] Collaborative Innovative Center of Chemical Science and Engineering (Tianjin), Tianjin 300072, China
[c] School of Physics & Materials Science, Anhui University, Hefei 230601, China

ABSTRACT

The utilization of solar energy into photoelectrochemical (PEC) water splitting is a popular approach to store the sustainable energy and minimize the dependence of fossil fuels. Herein, multi-layer $BiVO_4$ films were synthesized by multi-cycle electrodeposition following by annealing at high temperature. Multi-layer $BiVO_4$ films have monoclinic scheelite structure, and the morphology is changed from densely compact film to sponge-like network, and then bulk structure with the increase of electro-deposited layers. X-ray photoelectron spectra indicate the presence of abundant oxygen vacancies and V^{4+} species in multi-layer $BiVO_4$, especially for 3-layer one. For visible-light PEC performance, 3-layer $BiVO_4$ shows the highest photocurrent among the samples, i.e. up to 5.80 mA/cm^2 in sulfite oxidation and 1.79 mA/cm^2 in water splitting at 1.23 V versus a reverse hydrogen electrode (RHE) under 1 sun irradiation (100 mW/cm^2), with very high IPCE achieved nearly 83% and 25% (at 420 nm), respectively. The extremely high PEC performance of 3-layer $BiVO_4$ is attributed to its morphology of sponge-like network and the modulated band structure by the oxygen vacancies and V^{4+} species. Moreover, the multi-layer $BiVO_4$ also shows very high photostability. This work provides a multi-layer-construction method for highly visible-light-active PEC anodes for practical applications.

1. Introduction

With the increase of serious environment and energy-related issues around worldwide over the past decades, the strategy of harvesting and storing energy directly from solar light seems to be the most effective method to minimize the harmful impacts on the natural world [1–10]. Since Fujishima and Honda first discovered water photolysis on the TiO_2 photoelectrode [11], metal oxide semiconductor has been a hot topic in the applications of photocatalysis and photoelectrochemical (PEC) fields [12–19]. Among the metal oxides, n-type bismuth vanadate ($BiVO_4$) has recently emerged as a very promising photoanode for PEC water splitting, owing to its plentiful abundance, low cost, good stability, narrow bandgap energy (ca. 2.4 eV) for visible-light absorption, proper valence band (VB) edge located at ca. 2.4 V vs. reverse hydrogen electrode (RHE) for water oxidation (1.23 V vs. RHE), and a high theoretical photo-to-current conversion efficiency (η_{STH}) up to 9.3% with the maximum photocurrent of 7.6 mA/cm^2 under standard AM 1.5 G solar light illumination (100 mW/cm^2) [20–22].

Actually, $BiVO_4$ has two crystallographic forms: zircon-type structure and monoclinic scheelite structure [23], and the irreversibly transition from the former to the latter occurs at 397 °C–497 °C [24]. The monoclinic structure has a relative low band gap of 2.4 eV while the zircon-type one with 2.9 eV [25]. The monoclinic scheelite $BiVO_4$ was characterized by a layered structure containing cations with formal oxidation states of Bi^{3+} ($6s^2$) and V^{5+} ($3d^0$) in coordination with O^{2-} ($2p^6$) [26], and the local environment of Bi in the monoclinic scheelite structure is much more distorted than that in the zircon-type structure, which provides more opportunities for electron-hole separation and results in higher photoactivity [23]. Therefore, the most studied $BiVO_4$ materials are in monoclinic scheelite phase.

Even though, the actual conversion efficiency achieved with monoclinic $BiVO_4$ is far below what is expected, because it suffers from some drawbacks: (1) $BiVO_4$ has a short diffusion length lower than 100 nm [27], and a poor carrier mobility; (2) A high recombination (approximately 60%–80%) of photoinduced electron-hole pairs significantly restricts the PEC current [21,28]. Accordingly, during PEC

process, the photogenerated holes are mainly blocked in the bulk of $BiVO_4$ and consumed in the semiconductor/electrolyte interfaces before participating in the reaction of water oxidation to oxygen gas [29]. Up to now, many efforts have been done to improve the performance of $BiVO_4$, such as morphology control, facet engineering, metal and non-metal doping, *p-n* heterojunction, Z-scheme structure, *etc.* [20–22,30–34]. Among them, heteroatoms doping is one of the most used approach to photo-performance of $BiVO_4$, and the effective dopants include metal ions (*e.g.* Mo, W, Ti, Co) and nonmetal ions (*e.g.* P) [34–37]. Different from heteroatoms doping, oxygen vacancies and V^{4+} species, as an important class of dopant and shallow donors, could prevent photo-electrons and photo-holes from recombination, which will increase the photoactivity of the materials [38–40].

Herein, the approach of multi-cycle electrodeposition following by annealing at high temperature was applied to fabricate the multi-layer $BiVO_4$ photoanodes abundant with oxygen vacancies and V^{4+} species. With the increase of electrodeposited layers, the morphology changes from densely compacted film to sponge-like network, and then the bulk structure. During PEC test, 3-layer $BiVO_4$ shows the highest photocurrent of 5.80 mA/cm^2 in sulfite oxidation and 1.79 mA/cm^2 in water splitting at 1.23 V *versus* a reverse hydrogen electrode (RHE) under the light irradiation (100 mW/cm^2). Moreover, the multi-layer $BiVO_4$ also shows very high photostability.

2. Experimental section

2.1. Materials

$Bi(NO_3)_2$·H_2O, vanadyl acetylacetonate (VO(acac)$_2$), KI, acetone, *p*-benzoquinone, KOH and absolute ethanol were all obtained from Aladdin Chemicals. HNO$_3$ and dimethyl sulfoxide (DMSO) were gained from Tianjin Jiangtian Chemical Institute. Milli-Q ultrapure water (> 18 mΩ cm) was used in all experiments. All the reagents were analytical grade and used without further purification.

2.2. Sample preparation

2.2.1. Fabrication of BiOI film

As the precursor of $BiVO_4$, BiOI film was fabricated by electro-deposition (as shown in Scheme 1). First, a fluorine-doped tin oxide (FTO) coated glass were cleaned (with acetone, ethanol and water), and dried overnight, which was then used as electrode for BiOI deposition. The saturated Ag/AgCl electrode and Pt wire were applied as the reference electrode and counter electrode in all the electrodeposition process, respectively. 3.32 g KI was first dissolved in 50 mL Milli-Q ultrapure water (with its pH of 1.7), in which 0.97 g $Bi(NO_3)_2$·H_2O was added. The solution was mixed with 20 mL absolute ethanol solution involving 0.497 g *p*-benzoquinone under stirring for 30 min. After that, the electrodeposition was performed potentiostatically at −0.1 V *vs.* Ag/AgCl at room temperature for 3 min (According to previous work [22], the optimal deposition time was found to be 3–5 min. In this work, the deposition time of 3 min, 4 min and 5 min was compared, and the resulted $BiVO_4$ with 3-min deposition shows much better PEC current than 4 min and 5 min (Fig. S1, Supporting information, SI). Therefore, 3 min was set as one cycle for the preparation of BiOI film). On FTO substrate, *p*-benzoquinone can be reduced to hydroquinone, elevating the local pH and benefiting the precipitation of BiOI [41]. The electrodeposition process is repeated to obtain multi-layer BiOI films (from 1 to 6 layers, as shown in Scheme 1).

2.2.2. Synthesis of multi-layer BiVO$_4$

On the above prepared multi-layer BiOI electrode, 150 μL of a dimethyl sulfoxide (DMSO) solution containing 0.2 mol/L VO(acac)$_2$ was dripped. Subsequently, the samples were annealing at 450 °C for 2 h (with the increasing rate of 2 °C/min) in order to obtain the $BiVO_4$ in monoclinic phase. Afterwards, the film was soaking in 1.0 mol/L KOH to remove the excess V_2O_5 that present on the surface of $BiVO_4$. As shown in Scheme 1, the *x*-layer $BiVO_4$ was named as BV-*x* (*x* = 1–6).

2.3. Characterization

XRD patterns were recorded using D/MAX-2500 X-ray diffractometer equipped with Cu Kα radiation at 40 kV and 140 mA at a scanning rate of 5°/min. SEM images were observed using a field-emission scanning electron microscope (Hitachi, S-4800). High-resolution TEM observations were carried out with a Tecnai G^2 F-20 transmission electron microscope, and the energy dispersive spectrum (EDS) characterization was performed with an EDX system attached to TEM. X-ray photoelectron spectrum (XPS) was conducted with a PHI-1600 X-ray photoelectron spectroscope equipped with Al Kα radiation, and the
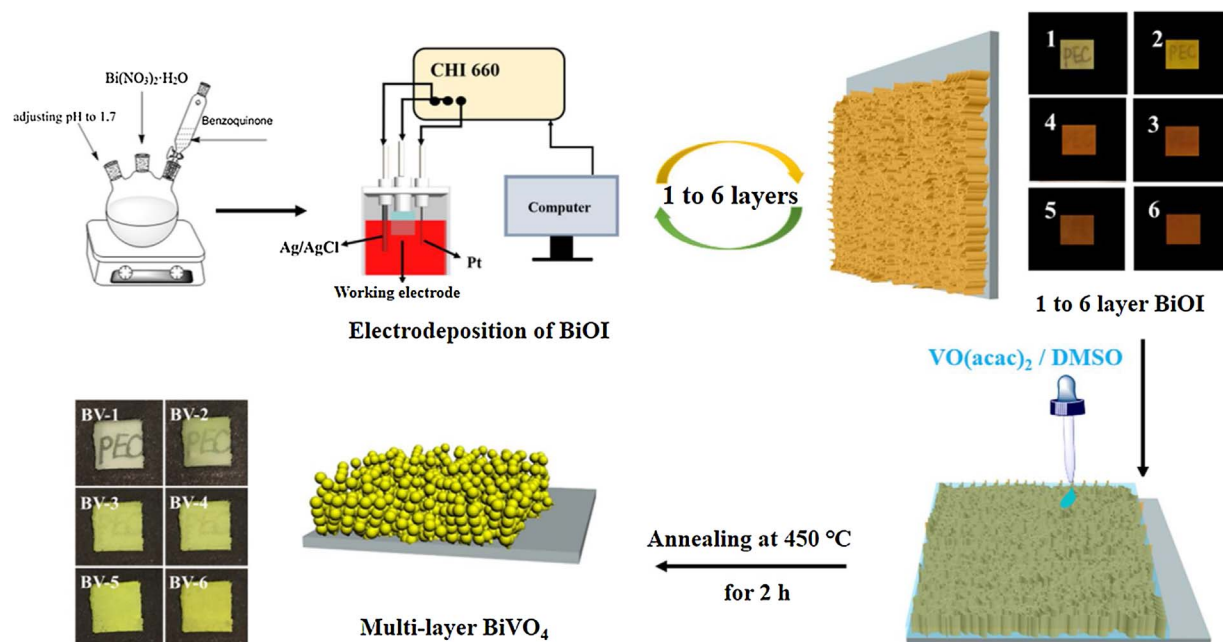
Scheme 1. Synthesis process of multi-layer BiVO$_4$.

binding energy was calibrated by the C1s peak (284.8 eV) of the contamination carbon. Raman spectra were recorded with a Raman spectrometer (DXR Microscope), and a green semiconductor laser (532 nm) was used as the excitation source. Steady-state photoluminescence (PL) spectra were measured by a Horiba Jobin Yvon Fluorolog 3–21 with the excitation light at 325 nm. UV–vis diffuse reflectance spectra (UV–vis DRS) were obtained from a Hitachi U-3010 spectrometer equipped with a 60 mm diameter integrating sphere using $BaSO_4$ as the reflectance sample.

2.4. Photoelectrochemical measurements

Photoelectrochemical (PEC) performances of multi-layer $BiVO_4$ photoanodes were evaluated in a typical three-electrode quartz cell with Pt wire as counter electrode and saturated Ag/AgCl as a reference electrode, using CHI 660E electrochemical workstation. The illumination source was a 300 W Xe arc lamp (100 mW/cm², PLS-SXE300UV, Beijing Trusttech. Co. Ltd).

The electrolyte for PEC sulfite oxidation is a 0.2 M Na_2SO_4 aqueous solution with 2 M Na_2SO_3 as hole scavenger (pH = 10), while 0.2 M Na_2SO_4 aqueous solution without hole scavenger (pH = 7) is for PEC water splitting. Linear sweep voltammetry (LSV) was monitored while sweeping the potential to the positive direction with a scan rate of 10 mV/s. The potential vs. Ag/AgCl reference electrode was converted to the potential vs. RHE according to the Nernst equation: E (vs. RHE) $= E$ (vs. Ag/AgCl) $+$ 0.0591 $\times$ pH $+$ 0.197 [3]. Electrochemical impedance spectroscopy (EIS) measurements were carried out with a sinusoidal ac perturbation of 10 mV applied over the frequency range of $0.01–10^5$ Hz.

The incident photon-to-current efficiency (IPCE) was calculated according to the following equation [22]:

$$IPCE(\lambda) = \frac{1240 \times J(\lambda)}{\lambda \times P(\lambda)} \times 100\%$$

where λ is the wavelength (nm), $J(\lambda)$ is the photocurrent density (mA/cm²), and $P(\lambda)$ is the incident power density of the monochromatic light (mW/cm²).

3. Results and discussion

3.1. Crystal structure and morphology

As shown in XRD patterns (Fig. 1a), all of as-prepared 1–6 layer $BiVO_4$ samples show the typical diffraction peaks of monoclinic scheelite $BiVO_4$ (JCPDS No. 14-0688, space group 15, C_{2h} [21]), and the characteristic peaks referring to SnO_2 (JCPDS No. 41-1445) are corresponding to FTO glass [22]. Compared with SnO_2 diffraction peaks, the higher layers of $BiVO_4$, from BV-1 to BV-6, exhibit sharper and more intense diffraction peaks, indicating the higher loading amount of $BiVO_4$ on FTO glass. Meanwhile, there are no other diffraction peaks attributed to other phases or impurities.

Furthermore, the crystal structure of monoclinic scheelite for the prepared $BiVO_4$ was also verified by Raman spectra (Fig. 1b), with the intense Raman bands at 124, 210, 330, 365, 720 and 827 cm⁻¹ [42–44]. The peaks at 124 and 210 cm⁻¹ are ascribed to the external modes of $BiVO_4$, while the peaks at 330 and 365 cm⁻¹ correspond to the asymmetric and symmetric deformation modes of the VO_4^{3-} tetrahedron ($\delta_{as}(VO^{3-})$ and $\delta_s(VO^{3-})$), respectively [42]. Moreover, the stretching modes of the vibrational modes of the V–O bands have been determined from the band centered at 827 cm⁻¹ (ν_s(V–O)) [42]. Similar to XRD results, the peak intensity of multi-layer $BiVO_4$ (from BV-1 to BV-6) becomes sharper and more intense, caused by the gradually increased loading amount of $BiVO_4$ on FTO glass.

Then, the surface morphology of multi-layer $BiVO_4$ was characterized by SEM and TEM. The electrodeposited BiOI (precursor of $BiVO_4$), shows typical two-dimensional morphology of a collection of randomly

oriented nanoflakes with voids between them, which provides higher surface area for introducing V sources into it (Fig. 2). There is a set of lattice fringes with an interval of 0.297 nm, which can be indexed to the (102) lattice plane of tetragonal BiOI.

After the introduction of V sources, i.e. VO(acac)₂, following by thermal annealing procedure, the morphologies of produced multi-layer $BiVO_4$ are shown in Fig. 3a–f (SEM images). With the layer increase, the thickness of $BiVO_4$ becomes thicker from 0.97 μm to 1.09 μm, 1.27 μm, 1.52 μm, 1.88 μm and 3.33 μm for BV-1, BV-2, BV-3, BV-4, BV-5 and BV-6, respectively (see the inset in Fig. 3a–f, and the serious aggregation is observed for BV-6). However, the surface features for the samples vary obviously with the layer thickened. BV-1 possesses a densely compacted layer assembled by $BiVO_4$ nanoparticles in size of ca. 200 nm. Two layers lead to the initial crystallization of $BiVO_4$ braches (BV-2), which then grow to sponge-like network assembled by randomly oriented nanorods for BV-3. However, further deposition of $BiVO_4$ layers (BV-4 and BV-5) will significantly enlarge the surface crystal size, make the surface much denser and cause the $BiVO_4$ in bulk size, and especially for BV-6, abundant bulk $BiVO_4$ particles (with the size more than 1 μm) cover the layer surface, which may inhibit the optical absorption and mass transfer for photoelectrochemical reaction.

With sponge-like network structure, BV-3 possesses porous crystal structure, which will provide more opportunities for light scattering inside and absorption, mass diffusion and electron transfer, benefiting the photoelectrochemical performance. According to TEM images (Fig. 3g), the nanorod on the surface of BV-3 has the chain structure linked by nanoparticles with the size of ca. 200 nm–400 nm. As shown in Fig. 3h, the spacing distance of 0.475 nm is in good accordance with the interplanar spacing of $BiVO_4$ (110) plane [45]. Moreover, the EDX mapping images (Fig. 3i) exhibits the homogeneous distribution of Bi, O and V elements in the nanorod, suggesting the purity of $BiVO_4$ layers.

3.2. Chemical state

X-ray photoelectron spectroscopy (XPS) was conducted to detect the surface chemical status of catalysts, and the survey spectra (Fig. S2, SI) only show the existence of Bi, V and O elements in BV-1, BV-3 and BV-5, indicating the purity of $BiVO_4$ in all samples. The high-resolution Bi 4f XPS spectra (Fig. 4a) reveal that the samples exhibit spin-orbit splitting signals of Bi 4f$_{7/2}$ and Bi 4f$_{5/2}$ at binding energy of ca. 164 eV and 159 eV, respectively, which are the characteristics of Bi^{3+} species [46]. Fig. 4b shows the doublet peaks located at binding energy about 524.0 eV and 516.5 eV in V 2p spectra, corresponding to V 2p$_{1/2}$ and V 2p$_{3/2}$, respectively, referring to V^{5+} cations in the crystal lattice [47]. Interestingly, BV-3 exhibits an obvious low-energy shift of Bi 4f and V 2p binding energies when compared with BV-1 and BV-5, which should be resulted from the presence of oxygen vacancies that may increase the electron density of Bi and V atoms [47]. Especially for V 2p spectra, V 2p$_{3/2}$ peak of BV-3 (Fig. 4c) can be fitted into two species of V^{5+} (516.5 eV) and V^{4+} (516.1 eV), and the latter V^{4+} is closely related to the existence of oxygen vacancies [29,48].

Moreover, the asymmetrical O 1s peak in the range of 527 eV–535 eV was fitted into three components centered at ca. 529.5, 530.3, 532.0 eV, as shown in Fig. 4d–f. The peaks located at 529.5 eV and 530.3 eV are attributed to O^{2-} at the lattice sites (O_L) and oxygen-vacancy regions (O_v), respectively [47], while the peak at 532.0 eV is assigned to chemisorbed oxygen and water (namely as O_A) [12]. It is worth noting that BV-3 possesses more oxygen vacancies than the other samples. The above results indicate the high-temperature annealing helps to create V^{4+} species in $BiVO_4$ lattice, during the reaction between BiOI and VO(acac)₂. Then, the partial reduction of V^{5+} to V^{4+} species leads to the formation of abundant oxygen vacancies as shallow donors [29].

The reason for higher concentration of V^{4+} species and oxygen vacancies in BV-3 than BV-1 and BV-5 may be attributed to its sponge-like network structure assembled by nanorods with higher surface
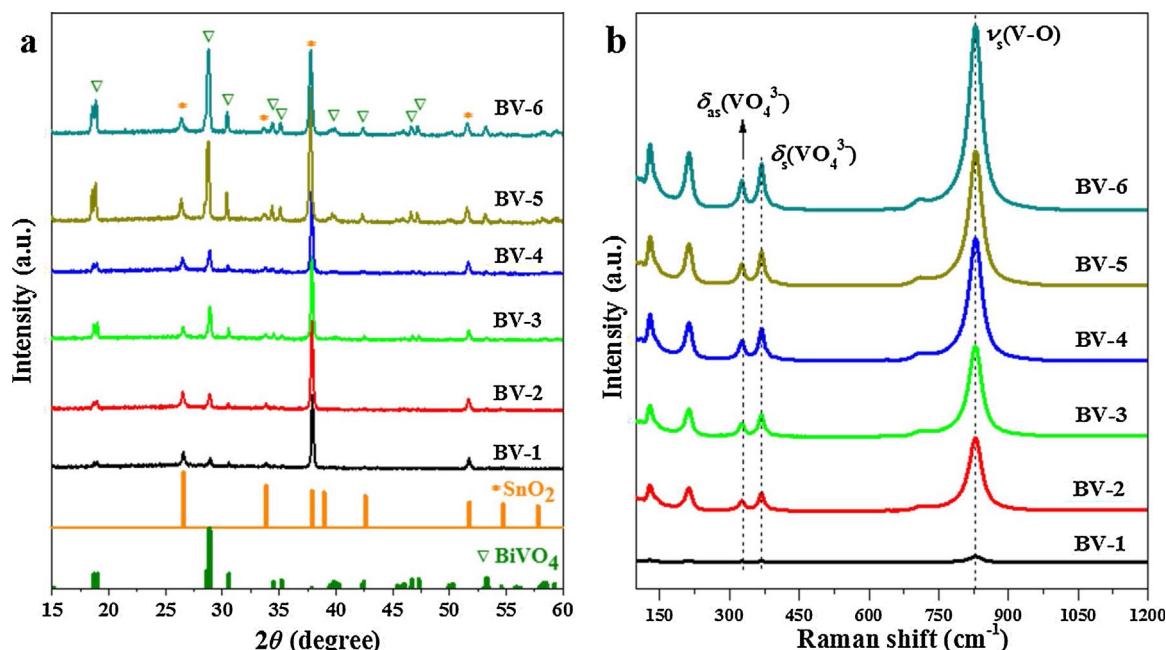
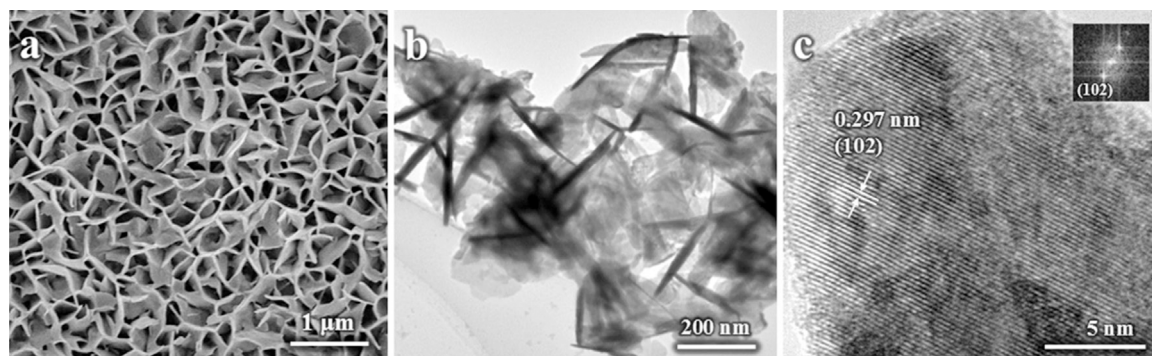**Fig. 1.** XRD patterns (a) and Raman spectra (b) of multi-layer BiVO$_4$ electrodes.

Fig. 2. SEM (a) and TEM images (b,c) of electrodeposited 1-layer BiOI.

exposed area for defects creation, while only compact surface and bulk structure are observed for BV-1 and BV-5, respectively. The presence of oxygen vacancies may be advantageous for the enhancement in photocatalytic and photoelectrochemical performance of the BiVO$_4$ material [29,47].

3.3. Optical properties

UV–vis absorption spectra of multi-layer BiVO$_4$ electrodes were tested and shown in Fig. 5a. All multi-layer BiVO$_4$ show visible-light absorption with the absorption edge at *ca.* 525 nm, and the PL emission peak at *ca.* 530 nm is also observed (Fig. S3, SI), attributed to the recombination of some extrinsic radiative transitions, such as charges recombination between the shallows level and intrinsic bands or recombination of donor-acceptor pairs [21].

Importantly, the optical absorption intensity in the range below 525 nm gradually increases from BV-1 to BV-3, and then decreases with further thicker layer (from BV-4 to BV-6). The highest visible-light absorption of BV-3 should be owing to its sponge-like network structure and surface defects (O$_v$ and V^{4+} species). Besides, the optical absorption near the band edge follows the formula $(\alpha h\nu) = a(h\nu - E_g)^n$, where α is absorption coefficient (which can be replace by absorbance (A)), $h\nu$ and E_g are respectively photon energy and band gap, a is a constant, and n is 1/2 for BiVO$_4$ with direct band gap [49]. The E_g value can be estimated by extrapolating the straight portion of $(Ah\nu)^2 - (h\nu)$ plot when A = 0. Thus, the calculated band gaps of multi-layer BiVO$_4$ except BV-3 are in the range of 2.45–2.46 eV, while BV-3 has a narrowed band gap of 2.42 eV. Then, the high-resolution VB (valence band) spectra of BV-1, BV-3 and BV-5 were conducted to get the exact value of VB edge (Fig. 5b), and it was found that the VB edge of all BiVO$_4$ samples is *ca.* 2.07 V (VB value from XPS spectra in Fig. 5b is 1.82 eV, and the work function of the instrument is 4.75 eV while that for normal hydrogen electrode (NHE) is 4.5 eV [50]). To exclude the effect of F:SnO$_2$ on the glass, we also tested its VB spectra, with the VB edge of *ca.* 3.35 eV (Fig. S4, SI). Therefore, the substrate of F:SnO$_2$ has no effects on the detection of BiVO$_4$ VB values. The result suggests the band-gap variation of BiVO$_4$ is resulted from the tuning of conduction band (CB) level. Accordingly, the band structures of BV-1, BV-3 and BV-5 are schemed in Fig. 5c. With the bulk BiVO$_4$ structure, BV-5 shows a band gap of 2.46 eV, while it decreases to 2.45 eV for BV-1 for the trace oxygen vacancies. Meanwhile, with the presence of abundant oxygen vacancies as well as V^{4+} species (a donor band [38]), BV-3 shows a much lower band gap of 2.42 eV.

3.4. Photoelectrochemical (PEC) properties

Photoelectrochemical (PEC) catalysis is emerging as one of the promising methods for solar hydrogen and oxygen generation, and has
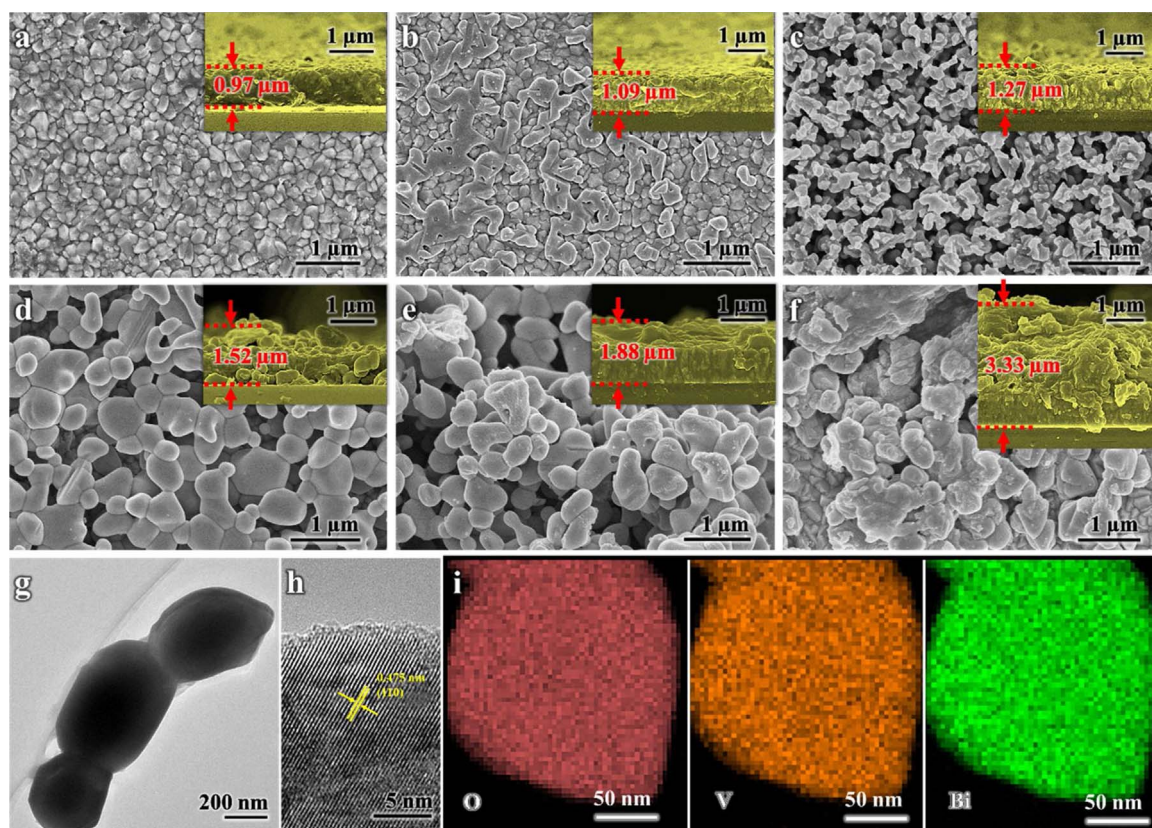
Fig. 3. SEM top view and cross-sectional view (inset in each figure) of multi-layer BiVO$_4$: (a) BV-1, (b) BV-2, (c) BV-3, (d) BV-4, (e) BV-5, (f) BV-6. TEM (g), HR-TEM (h) and EDX mapping images (i) of BV-3.
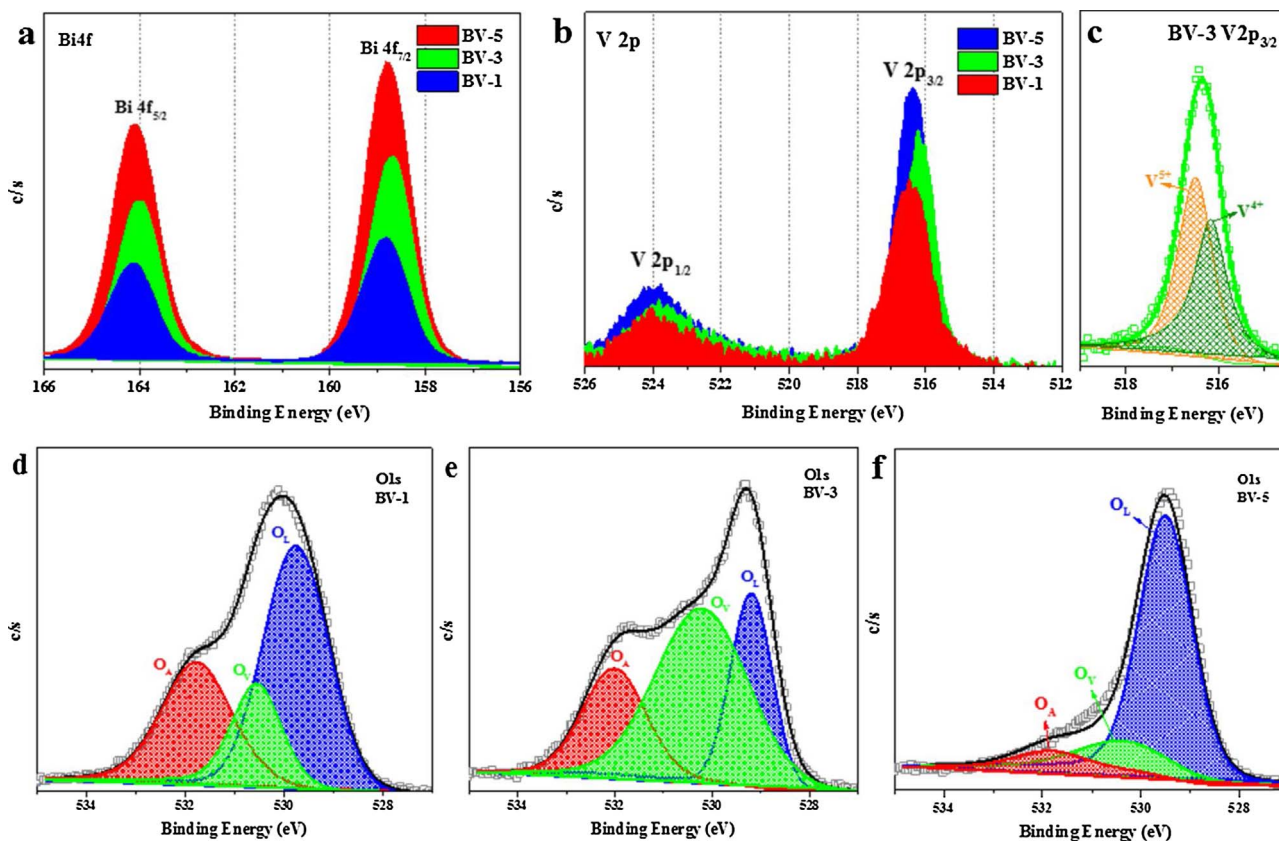

Fig. 4. XPS spectra of BV-1, BV-3 and BV-5. (a) Bi 4f, (b) V 2p, (c) V 2p$_{3/2}$ of BV-3, (d-f) O 1s spectra.
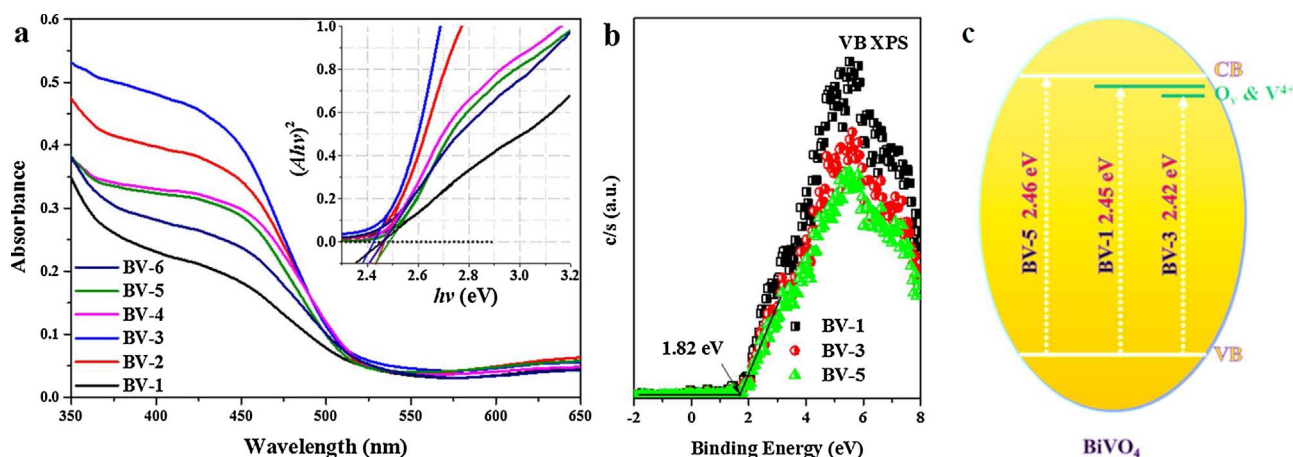
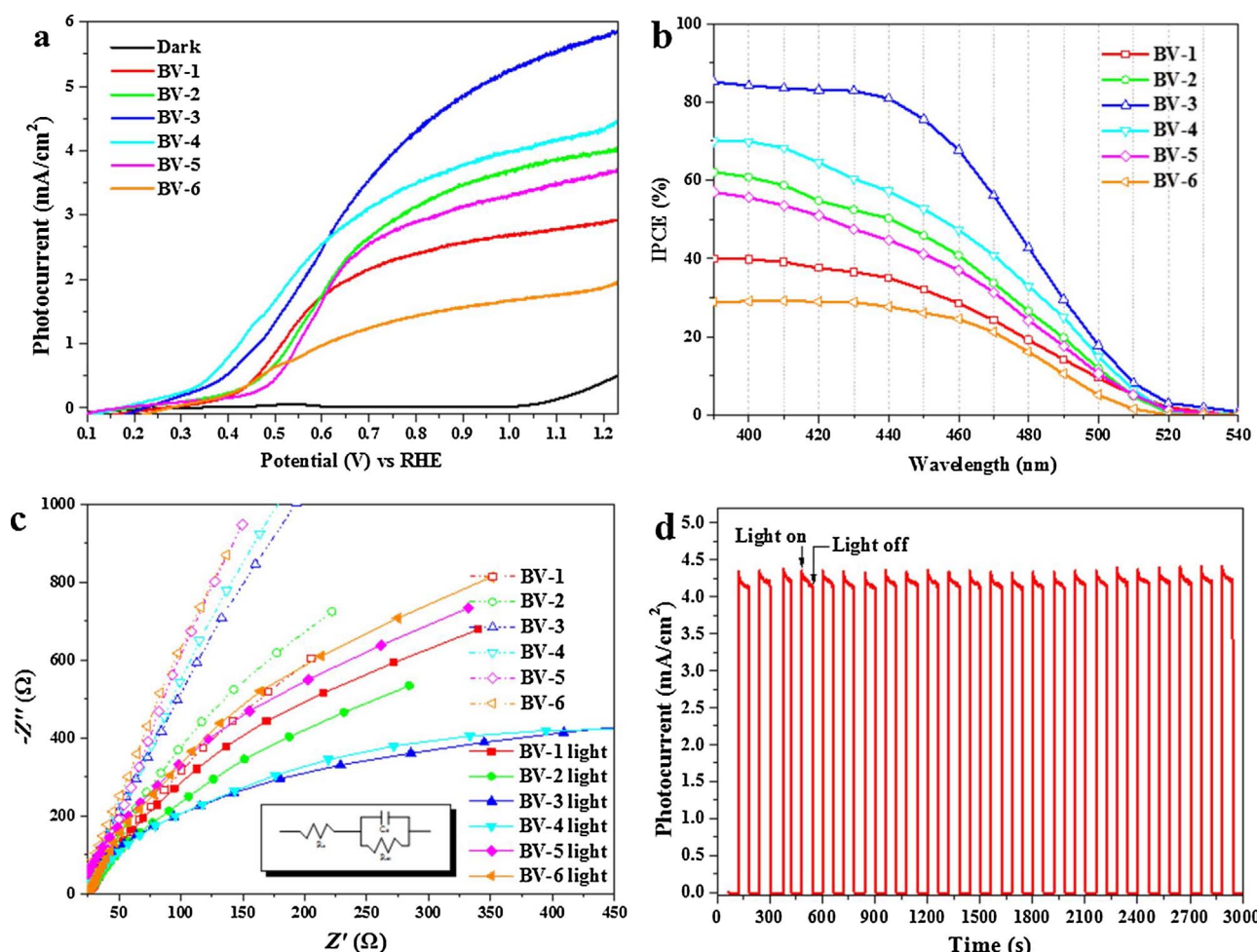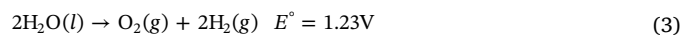**Fig. 5.** UV–vis absorption (a), high-resolution VB XPS spectra (b) and band structure (c) of multi-layer BiVO$_4$.
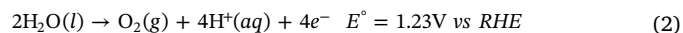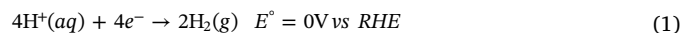

Fig. 6. PEC properties of multi-layer BiVO$_4$ electrodes for sulfite oxidation in a 0.2 M Na$_2$SO$_4$/2 M Na$_2$SO$_3$ aqueous solution at pH = 10 under light illumination (100 mW/cm^2). (a) *J-V* curves. (b) Incident photon to current efficiency (IPCE) at 1.1 V *vs* RHE. (c) Electrochemical impedance spectroscopy (EIS, in dark and under light irradiation) and (d) PEC stability (0.8 V *vs*. RHE) of BV-3. Inset in (c): EIS fitting model, R_s, electrolyte resistance; R_{ct}, charge-transfer resistance; C_d, capacitive reactance).

attracted increasing interest [21]. The PEC water splitting involves separating the oxidation and reduction processes into half-cell reactions (Eqs. (1) and (2)), and Eq. (3) shows the overall reaction. However, the kinetics for oxygen evolution is very slow relative to sulfite oxidation, as shown in Eq. (4). The surface recombination of sulfite oxidation is negligible and Φ_{ox} (the yield of the surface reaching holes that are injected into the solution species) is ~100% [21]. Therefore, measuring photocurrent for sulfite oxidation enables investigation of the PEC properties of BiVO$_4$ independently of its poor water oxidation kinetics [22].

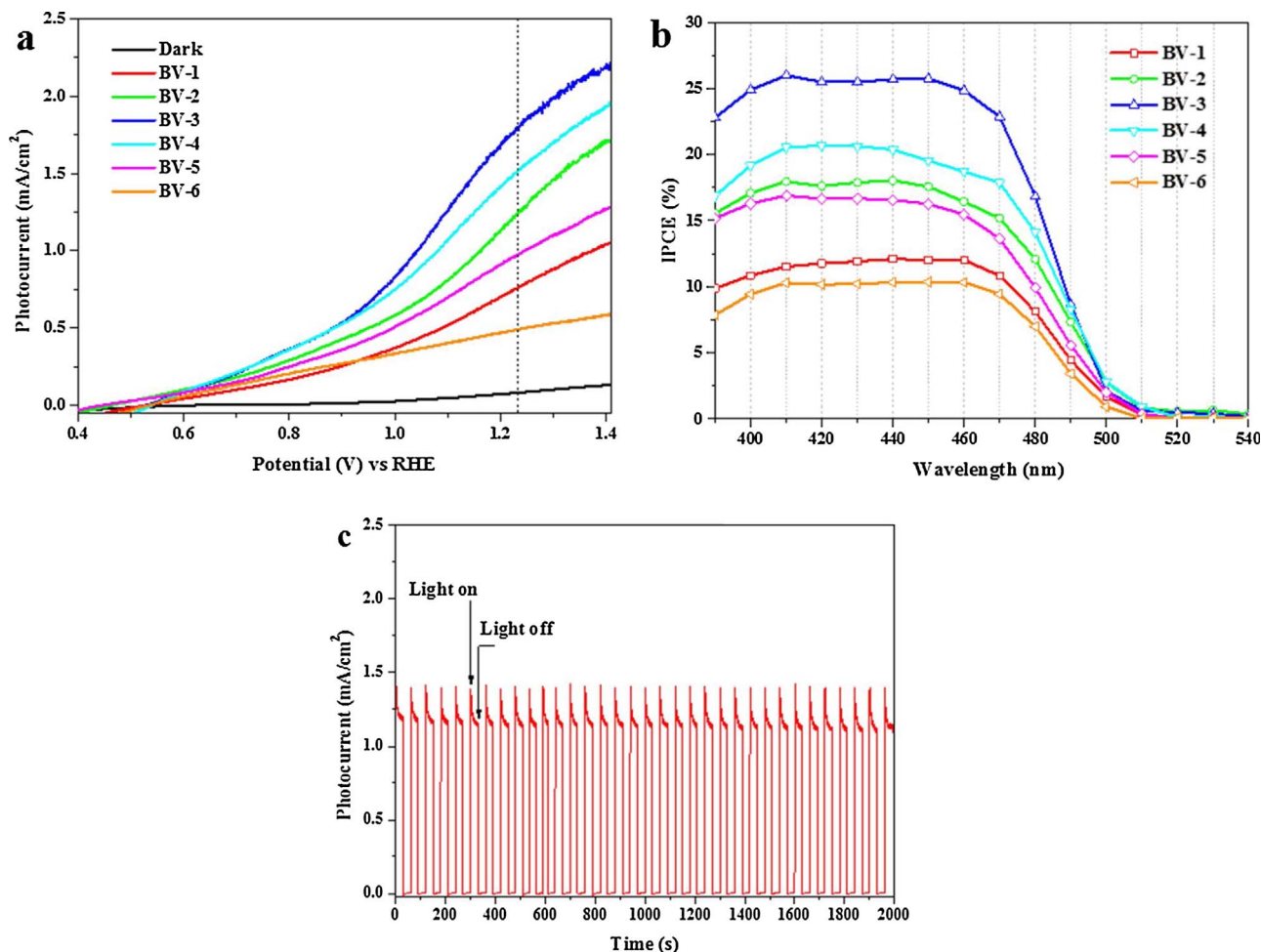$$4H^+(aq) + 4e^- \rightarrow 2H_2(g) \quad E^\circ = 0V \text{ vs RHE} \tag{1}$$

$$2H_2O(l) \rightarrow O_2(g) + 4H^+(aq) + 4e^- \quad E^\circ = 1.23V \text{ vs RHE} \tag{2}$$

$$2H_2O(l) \rightarrow O_2(g) + 2H_2(g) \quad E^\circ = 1.23V \tag{3}$$

Fig. 7. PEC properties of multi-layer BiVO$_4$ electrodes for water splitting in a 0.2 M Na$_2$SO$_4$ aqueous solution at pH = 7 under light illumination (100 mW/cm^2). (a) *J-V* curves, (b) IPCE at 1.1 V *vs* RHE, and (c) PEC stability (1.1 V *vs.* RHE) of BV-3.

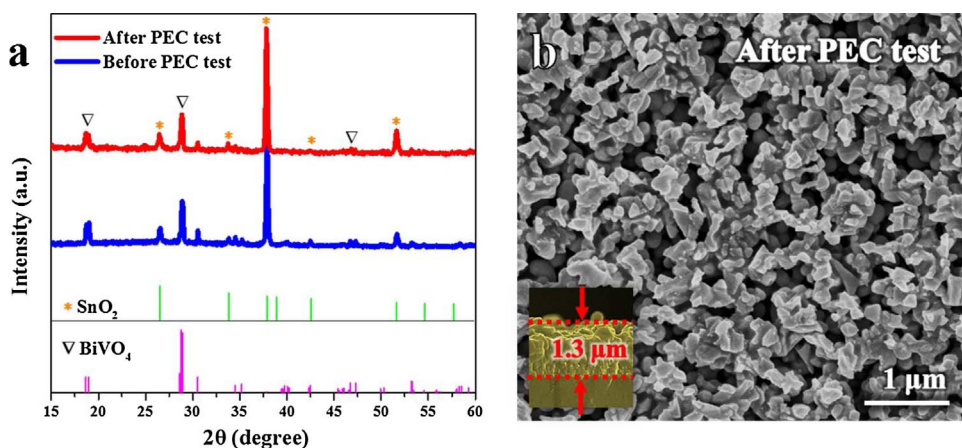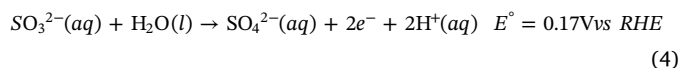**Fig. 8.** (a) XRD patterns and (b, c) SEM images of BV-3 before and after PEC water splitting reaction.

$$SO_3{}^{2-}(aq) + H_2O(l) \rightarrow SO_4{}^{2-}(aq) + 2e^- + 2H^+(aq) \quad E^\circ = 0.17V vs\ RHE \tag{4}$$

Therefore, the PEC properties for sulfite oxidation of the multi-layer BiVO$_4$ were measured by using Na$_2$SO$_3$ as hole scavenger. As shown in Fig. 6a, the multi-layer BiVO$_4$ show no current in dark. When under AM 1.5 G illumination (100 mW/cm^2), the on-set potential for multi-layer BiVO$_4$ is very early, *i.e.* 0.1 V–0.2 V *vs.* RHE. Moreover, BV-1 exhibits a photocurrent of 3.0 mA/cm^2 at the potential of 1.23 V *vs.* RHE. Then, the PEC activity increases sharply from one layer to two (BV-2, 4.0 mA/

cm^2) and three BiVO$_4$ layers (BV-3, 5.8 mA/cm^2), but decreases with further four, five and six layers (BV-4, 4.33 mA/cm^2; BV-5, 3.64 mA/cm^2; and BV-6, 1.88 mA/cm^2). Importantly, the extremely high photocurrent of BV-3 is *ca.* 76.3% of the theoretical one (7.6 mA/cm^2).

Then, the incident photon-to-current conversion efficiency (IPCE) of multi-layer BiVO$_4$ was analyzed (Fig. 6b). The wavelength of the initial light response of samples are all below *ca.* 520 nm (which is almost the band gap of BiVO$_4$), and the IPCE increases gradually when reducing the irradiation-light wavelength. Among the samples, BV-3 shows much higher IPCE than others, with its value up to 83% (at 420 nm). The

activity trend from IPCE is BV-3 > BV-4 > BV-2 > BV-5 > BV-1 > BV-6, the same trend with PEC current (*J-V* curves).

Moreover, in electrochemical impedance spectroscopy (EIS), the arc radius of Nyquist plots can be used to evaluate the charge transfer resistance at the semiconductor/electrolyte interface, smaller arc radius implies smaller charge transfer resistance [14]. From EIS plots (Fig. 6c), the charge transfer resistance of the samples was calculated based on fitting model (see the inset in Fig. 6c). In dark, the charge transfer resistance (R_{ct}) is in the order of R_{ct}(BV-6, 225.4 Ω) ≈ R_{ct}(BV-5, 185.2 Ω) > R_{ct}(BV-4, 178.7 Ω) > R_{ct}(BV-3, 176.3 Ω) > R_{ct}(BV-2, 172.1 Ω) > R_{ct}(BV-1, 167.8 Ω), which is corresponding to the layer thickness of $BiVO_4$ (*i.e.* thick layer leads to higher R_{ct}). However, under light irradiation, the charge transfer resistances for all samples are decreased obviously, and the order is also altered significantly, *i.e.*, R_{ct}(BV-6, 218.8 Ω) > R_{ct}(BV-5, 175.7 Ω) > R_{ct}(BV-1, 161.4 Ω) > R_{ct}(BV-2, 160.5 Ω) > R_{ct}(BV-4, 159.3 Ω) > R_{ct}(BV-3, 137 Ω), indicating the high conductivity of BV-3 and BV-4 owing to the oxygen vacancy in the surface. Therefore, the improved conductivity of $BiVO_4$ will make electrons rapidly transferred, which then reduce the recombination of photoexcited holes with electrons. Thus, a low onset potential and a high photocurrent can be observed for BV-3 and BV-4 [51,52]. The light-induced R_{ct} variations are 6.4, 11.6, 39.3, 19.4, 9.5 and 6.6 Ω for BV-1 to BV-6, respectively. Among the samples, BV-3 exhibits the most active response to solar light, which is correlated to the PEC performance. Besides, BV-3 also exhibits high PEC stability with a very steady photocurrent more than 3000 s (Fig. 6d).

Furthermore, the PEC properties for water splitting of the multi-layer $BiVO_4$ were measured in 0.2 M Na_2SO_4 aqueous solution, as shown in Fig. 7. The PEC activity of the samples in water splitting is lower than that in sulfite oxidation, because the latter is thermodynamically and kinetically more facile than the former [21,22]. In PEC water splitting (Fig. 7a), the multi-layer $BiVO_4$ shows no current in dark. Under light illumination (100 mW/cm^2), BV-1 exhibits a photocurrent of 0.76 mA/cm^2 at the potential of 1.23 V *vs.* RHE. Then, the PEC activity increases sharply from one layer to two (BV-2, 1.24 mA/cm^2) and three $BiVO_4$ layers (BV-3, 1.79 mA/cm^2), but decreases with further four, five and six layer $BiVO_4$ (BV-4, 1.51 mA/cm^2; BV-5, 0.97 mA/cm^2; and BV-6, 0.49 mA/cm^2).

Then, IPCE for PEC water splitting was analyzed (Fig. 7b), which shows the similar trend with sulfite oxidation (Fig. 6b), *i.e.*, the wavelengths of the light response are below *ca.* 520 nm, and the IPCE increases gradually with the decrease of irradiation-light wavelength. Especially for BV-3, it shows much higher IPCE than others, with its value higher than 25% (at 420 nm). The activity trend from IPCE is BV-3 > BV-4 > BV-2 > BV-5 > BV-1 > BV-6. Also, BV-3 also possesses very high photostability without obvious decrease of PEC current (Fig. 7c). After PEC test (over 3 h), BV-3 shows the same X-ray diffraction peaks (XRD patterns in Fig. 8a) and almost similar surface morphology of sponge-like network (SEM images in Fig. 8b and c) with the fresh one, also confirming the high photostability of multi-layer $BiVO_4$.

Among the multi-layer $BiVO_4$ photoanodes, BV-3 shows the highest PEC activity and IPCE in sulfite oxidation and water splitting. The reason for that should be the sponge-like network structure for better mass transfer and light absorption (and light scattering in network), and the defects of O_v and V^{4+} for lowering band gap, enhancing the carrier density, reducing surface Fermi level pinning effect [29], and then improving the charge-separation efficiency (η_{sep}) and charge-transfer efficiency (η_{trans}).

4. Conclusions

The multi-layer $BiVO_4$ films were synthesized by multi-cycle electrodeposition following by high-temperature annealing, which all possess monoclinic scheelite structure. The morphology for sponge-like network is obtained for 3-layer $BiVO_4$, which also has abundant oxygen

vacancies and V^{4+} species in crystal lattice, which benefits the light absorption, mass and charge transfer. Therefore, 3-layer $BiVO_4$ shows the highest photocurrent in PEC tests, *i.e.* up to 5.80 mA/cm^2 in sulfite oxidation and 1.79 mA/cm^2 in water splitting at 1.23 V *versus* RHE under light irradiation (100 mW/cm^2), with IPCE achieved nearly 83% and 25% (at 420 nm), respectively. The high PEC performance of 3-layer $BiVO_4$ should be attributed to its sponge-like network, and abundant defects of oxygen vacancies and V^{4+} species. Moreover, the multi-layer $BiVO_4$ also shows very high photostability in PEC sulfite oxidation and water splitting. This work provides an effective method to fabricate highly visible-light-active multi-layer PEC anodes for practical applications.

Appendix A. Supplementary data

Supplementary data associated with this article can be found, in the online version, at http://dx.doi.org/10.1016/j.apcatb.2017.09.031.

References

[1] Y. Bai, I. Mora-Seró, F. De Angelis, J. Bisquert, P. Wang, Chem. Rev. 114 (2014) 10095–10130.
[2] D. Kang, T.W. Kim, S.R. Kubota, A.C. Cardiel, H.G. Cha, K.-S. Choi, Chem. Rev. 115 (2015) 12839–12887.
[3] L. Pan, S. Wang, J. Xie, L. Wang, X. Zhang, J.-J. Zou, Nano Energy 28 (2016) 296–303.
[4] L. Ma, H. Han, L. Pan, M. Tahir, L. Wang, X. Zhang, J.-J. Zou, RSC Adv. 6 (2016) 63984–63990.
[5] C.R. Lhermitte, B.M. Bartlett, Acc. Chem. Res. 49 (2016) 1121–1129.
[6] M. Tahir, L. Pan, F. Idrees, X. Zhang, L. Wang, J.-J. Zou, Z.L. Wang, Nano Energy 37 (2017) 136–157.
[7] L. Pan, S. Wang, W. Mi, J. Song, J.-J. Zou, L. Wang, X. Zhang, Nano Energy 9 (2014) 71–79.
[8] T. Hisatomi, J. Kubota, K. Domen, Chem. Soc. Rev. 43 (2014) 7520–7535.
[9] S. Fang, Y. Xia, K. Lv, Q. Li, J. Sun, M. Li, Appl. Catal. B: Environ. 185 (2016) 225–232.
[10] H. Yu, P. Xiao, J. Tian, F. Wang, J. Yu, ACS Appl. Mater. Interfaces 8 (2016) 29470–29477.
[11] A. Fujishima, K. Honda, Nature 238 (1972) 37–38.
[12] L. Pan, T. Muhammad, L. Ma, Z.-F. Huang, S. Wang, L. Wang, J.-J. Zou, X. Zhang, Appl. Catal. B: Environ. 189 (2016) 181–191.
[13] S. Wang, X. Zhang, S. Li, Y. Fang, L. Pan, J.-J. Zou, J. Hazard. Mater. 331 (2017) 235–245.
[14] S. Wang, L. Pan, J.-J. Song, W. Mi, J.-J. Zou, L. Wang, X. Zhang, J. Am. Chem. Soc. 137 (2015) 2975–2983.
[15] Z.a. Huang, Q. Sun, K. Lv, Z. Zhang, M. Li, B. Li, Appl. Catal. B: Environ. 164 (2015) 420–427.
[16] R. Yang, J. Cai, K. Lv, X. Wu, W. Wang, Z. Xu, M. Li, Q. Li, W. Xu, Appl. Catal. B: Environ. 210 (2017) 184–193.
[17] W. Fan, C. Li, H. Bai, Y. Zhao, B. Luo, Y. Li, Y. Ge, W. Shi, H. Li, J. Mater. Chem. A 5 (2017) 4894–4903.
[18] W. Fan, C. Chen, H. Bai, B. Luo, H. Shen, W. Shi, Appl. Catal. B: Environ. 195 (2016) 9–15.
[19] Z.-F. Huang, J. Song, L. Pan, X. Jia, Z. Li, J.-J. Zou, X. Zhang, L. Wang, Nanoscale 6 (2014) 8865–8872.
[20] C. Liu, J. Su, J. Zhou, L. Guo, ACS Sustain. Chem. Eng. 4 (2016) 4492–4497.
[21] Z.-F. Huang, L. Pan, J.-J. Zou, X. Zhang, L. Wang, Nanoscale 6 (2014) 14044–14063.
[22] T.W. Kim, K.-S. Choi, Science 343 (2014) 990–994.
[23] Y. Park, K.J. McDonald, K.S. Choi, Chem. Soc. Rev. 42 (2013) 2321–2337.
[24] A. Kudo, K. Omori, H. Kato, J. Am. Chem. Soc. 121 (1999) 11459–11467.
[25] S. Hernández, G. Gerardi, K. Bejtka, A. Fina, N. Russo, Appl. Catal. B: Environ. 190 (2016) 66–74.
[26] J.K. Cooper, S. Gul, F.M. Toma, L. Chen, P.-A. Glans, J. Guo, J.W. Ager, J. Yano, I.D. Sharp, Chem. Mater. 26 (2014) 5365–5373.
[27] M.G. Lee, D.H. Kim, W. Sohn, C.W. Moon, H. Park, S. Lee, H.W. Jang, Nano Energy 28 (2016) 250–260.
[28] K. Sivula, R. van de Krol, Nat. Rev. Mater. 1 (2016) 15010.
[29] S. Wang, P. Chen, J.-H. Yun, Y. Hu, L. Wang, Angew. Chem. Int. Ed. 56 (2017) 8500–8504.

[30] R. Li, F. Zhang, D. Wang, J. Yang, M. Li, J. Zhu, X. Zhou, H. Han, C. Li, Nat. Commun. 4 (2013) 1432.

[31] Y. Kuang, Q. Jia, H. Nishiyama, T. Yamada, A. Kudo, K. Domen, Adv. Energy Mater. 6 (2016) 1501645.

[32] F. Chen, Q. Yang, X. Li, G. Zeng, D. Wang, C. Niu, J. Zhao, H. An, T. Xie, Y. Deng, Appl. Catal. B: Environ. 200 (2017) 330–342.

[33] W. Zhao, Y. Liu, Z. Wei, S. Yang, H. He, C. Sun, Appl. Catal. B: Environ. 185 (2016) 242–252.

[34] B. Zhang, H. Zhang, Z. Wang, X. Zhang, X. Qin, Y. Dai, Y. Liu, P. Wang, Y. Li, B. Huang, Appl. Catal. B: Environ. 211 (2017) 258–265.

[35] A.J.E. Rettie, H.C. Lee, L.G. Marshall, J.-F. Lin, C. Capan, J. Lindemuth, J.S. McCloy, J. Zhou, A.J. Bard, C.B. Mullins, J. Am. Chem. Soc. 135 (2013) 11389–11396.

[36] Y. Zhu, M.W. Shah, C. Wang, Appl. Catal. B: Environ. 203 (2017) 526–532.

[37] W.J. Jo, J.-W. Jang, K.-j. Kong, H.J. Kang, J.Y. Kim, H. Jun, K.P.S. Parmar, J.S. Lee, Angew. Chem. Int. Ed. 51 (2012) 3147–3151.

[38] L. Pan, S. Wang, J.-J. Zou, Z.-F. Huang, L. Wang, X. Zhang, Chem. Commun. 50 (2014) 988–990.

[39] L. Pan, J.-J. Zou, S. Wang, X.-Y. Liu, X. Zhang, L. Wang, ACS Appl. Mater. Interfaces 4 (2012) 1650–1655.

[40] L. Pan, X. Zhang, L. Wang, J.-J. Zou, Mater. Lett. 160 (2015) 576–580.

[41] K.J. McDonald, K.-S. Choi, Energy Environ. Sci. 5 (2012) 8553–8557.

[42] H. Yoon, M.G. Mali, J.Y. Choi, M.W. Kim, S.K. Choi, H. Park, S.S. Al-Deyab, M.T. Swihart, A.L. Yarin, S.S. Yoon, Langmuir 31 (2015) 3727–3737.

[43] G. Li, D. Zhang, J.C. Yu, Chem. Mater. 20 (2008) 3983–3992.

[44] P. Madhusudan, J. Ran, J. Zhang, J. Yu, G. Liu, Appl. Catal. B: Environ. 110 (2011) 286–295.

[45] S. Dong, J. Feng, Y. Li, L. Hu, M. Liu, Y. Wang, Y. Pi, J. Sun, J. Sun, Appl. Catal. B: Environ. 152–153 (2014) 413–424.

[46] S. Gu, W. Li, F. Wang, S. Wang, H. Zhou, H. Li, Appl. Catal. B: Environ. 170–171 (2015) 186–194.

[47] H. Jiang, H. Dai, X. Meng, L. Zhang, J. Deng, K. Ji, Chin. J. Catal. 32 (2011) 939–949.

[48] Y. Zhu, W. Lu, H. Li, H. Wan, J. Catal. 246 (2007) 382–389.

[49] C. Lv, J. Sun, G. Chen, Y. Zhou, D. Li, Z. Wang, B. Zhao, Appl. Catal. B: Environ. 208 (2017) 14–21.

[50] Z. Xiong, L.L. Zhang, J. Ma, X.S. Zhao, Chem. Commun. 46 (2010) 6099–6101.

[51] M. Li, J. Deng, A. Pu, P. Zhang, H. Zhang, J. Gao, Y. Hao, J. Zhong, X. Sun, J. Mater. Chem. A 2 (2014) 6727–6733.

[52] M. Ma, K. Zhang, P. Li, M.S. Jung, M.J. Jeong, J.H. Park, Angew. Chem. Int. Ed. 55 (2016) 11819–11823.